Vert Belenguer, VB.; Melo Faus, FV.; Navarrete Algaba, L.; Serra Alfaro, JM. (2012). Redox stability and electrochemical study of nickel doped chromites as anodes for H-2/CH4-fueled solid oxide fuel cells. Applied Catalysis B Environmental. 115:346-356. https://doi.org/10.1016/j.apcatb.2011.12.033

Redox Stability and Electrochemical Study of Nickel Doped Chromites as Anodes for H_2/CH_4-Fueled Solid Oxide Fuel Cells

Applied Catalysis B: Environmental 115– 116 (2012) 346– 356 (doi: 10.1016/j.apcatb.2011.12.033)

Vicente B. Vert, Francisco V. Melo, Laura Navarrete, José M. Serra[*]

Instituto de Tecnología Química (Universidad Politécnica de Valencia – Consejo Superior de Investigaciones Científicas), Av. Los Naranjos, s/n – Building 6C Campus UPV 46022 Valencia (Spain)

[*] corresponding author: e-mail: jmserra@itq.upv.es; phone: +34.963879448

ABSTRACT: The influence of nickel and strontium incorporation in $LaCrO_3$ on the crystalline structure, redox behavior and electrochemical performance by impedance spectroscopy using symmetrical cells has been studied. Namely, the $La_{1-x}Sr_xCr_{1-y}Ni_yO_{3-\delta}$ (x=0, 0.15; y=0.05, 0.1, 0.2) system was investigated. Structural and redox evolution has been monitored by X-ray diffraction in oxidized and reduced samples. Reduced samples kept the initial perovskite structure although metallic nickel nanoparticles were detected on the perovskite grain surface by TEM analysis. The re-oxidized surface did not present nickel particles, suggesting the nickel re-incorporation into perovskite lattice coupled with cation diffusion. The perovskites were tested as SOFC anodes and the polarization resistance depended on the nickel stoichiometry and the reduction temperature. $La_{0.85}Sr_{0.15}Cr_{0.9}Ni_{0.1}O_{3-\delta}$ reduced at 800ºC showed the lowest polarization resistance, both in hydrogen and methane. In fact this composition showed a 20% methane conversion at 900 ºC for the methane steam reforming in a fixed bed reactor. Tolerance to redox cycling was proved electrochemically by in-situ treatments of $La_{0.85}Sr_{0.15}Cr_{0.9}Ni_{0.1}O_{3-\delta}$ electrode. Materials were further analyzed by TPR and XPS (in oxidized and reduced state) in order to identify the possible species involved in the electrocatalytic processes.

Keywords: *Anode, Chromites, Redox Cycle, nickel, nanoparticle, redox cycling, Methane Steam Reforming*

1. INTRODUCTION

Energy production from cleaner sources is becoming a major issue for large scale economies. Fuel cells are interesting energy conversion devices because of the low pollutant emission and high efficiency. Among the different fuel cell types, solid oxide fuel cells (SOFCs) operating at high temperatures are one of the most promising systems for extensive energy production [1] for stationary applications. Hydrogen is the most efficient and environmental-friendly fuel, however, it is difficult to transport and should be produced from electricity or fossil resources [2, 3, 4, 5]. The implementation of SOFC stacks, which operate directly with other more available fuels, like natural gas, biogas or bioalcohols, is becoming of great interest for widening the fuel cell applicability. Beside the high efficiency, modularity and noiseless operation of SOFC systems, the use of hydrocarbon fuels in SOFC produces an exhaust stream free of nitrogen and principally made of H_2O and CO_2. This CO_2 can readily be separated and liquefied, and consequently the CO_2 emissions in the power generation process can be minimized. Conventional SOFC anodes are based on nickel and yttria stabilized zirconia (8YSZ) composites. The high catalytic activity of nickel for the conversion of hydrocarbons is combined with high ionic-electronic conductivities (at high temperatures) in this cermet anode. However, the high anode nickel content catalyzes the formation of carbon deposits or oxidizes at high steam concentrations. These problems could be circumvented with a well-engineered balance of plant (BoP) in the SOFC-system although the oxidation risk (high –local- steam concentration) would be still an issue for operation at high fuel utilization. The catalytic activity and conductivity of Ni-8YSZ anodes decreases under hydrocarbon atmospheres because of coking. Regeneration of this type of anodes is not feasible due to redox instability which results in the mechanical failure upon nickel oxidation [6]. Several alternative metals have been proposed as hydrocarbon activation electrocatalysts, i.e., Cu, Ru, Pt, Pd, Rh [7]. Nonetheless, combined low-cost, stability and catalytic activity is still a critical issue. A possible alternative is to replace the anode cermet by an ionic conductor like gadolinium doped ceria (GDC). Under reducing atmospheres the GDC material acts as a mixed ionic-electronic conductor [8, 9] (MIEC) but the total conductivity is still low. Metals must be added onto GDC surface in order to increase electrical conductivity and catalytic activity and the cermet regeneration problem comes up again. Moreover, ceria reduction in reducing conditions results in acute expansion processes, which can result in the mechanical failure due to the expansion mismatch with other cell components.

Titanates and chromites are single-phased perovskite (ABO_3) materials, which are stable under reducing atmospheres [10, 11, 12]. An adequate doping of these perovskites can maintain the stability and provide enough oxygen (O^{2-}) and electrical conductivity for acting as SOFC anodes. Nevertheless, titanates have shown lower electrocatalytic activity than chromites [8].

In the case of chromites, the $LaCrO_3$ material is commonly used as interconnector in SOFC due to its high stability and high conductivity under reducing (and oxidizing) atmospheres. Further Sr doping increases conductivity and reduces the sintering temperature by forming liquid phases like $SrCrO_4$ [13]. The presence of divalent cations increases the number of oxygen vacancies and enhances the ionic conductivity. A higher electrocatalytic activity is achieved by introducing other elements (Ni, Co, Mg, Ru or V [14, 15]) either in the perovskite lattice by partial substitution of chromium or on the grain surface by impregnation/infiltration. In addition, other lanthanides seem to improve the redox stability, conductivity and electrocatalysis of nickel-doped chromites, as stated for $Pr_{0.7}Sr_{0.3}Cr_{0.9}Ni_{0.1}O_{3-\delta}$ [16].

In this work, strontium-lanthanum chromites have been doped with different nickel contents in the $La_{1-x}Sr_xCr_{1-y}Ni_yO_{3-\delta}$ system. Different characterization techniques have been used for determining the influence of nickel (and strontium) content on the structure, oxidation state of the rest of lattice cations, overall redox behavior and fuel activation. The different electrode compositions have been tested as anodes in symmetrical cells under different wet hydrogen or methane atmospheres while the activity towards methane steam reforming has been tested in a fixed bed reactor. Finally, the redox cyclability has been studied on a selected Ni-containing chromite electrode by electrochemical analysis subjected to in-situ environment cycling from air to hydrogen, aiming to prove the regenerability of this kind of electrodes.

2. EXPERIMENTAL

Perovskite materials have been synthesized by Pechini method, i.e. citrate complexation followed by pyrolysis and calcination [17, 18, [19]]. Several calcinations steps were necessary in order to minimize the presence of impurities, i.e. upon calcination at 1050 ºC for 10 h of the foam precursor obtained by complexation-polymerization, the powders were consecutively calcined at 1100, 1150 and 1200 ºC for 12 h each in air in covered alumina crucibles. A direct treatment at 1200 ºC for 12-24 h allowed obtaining only minor amounts of $SrCrO_4$, although the complex thermal treatment make it possible to reduce more the presence of this secondary phase. As-calcined powders were milled with 3YSZ (Tosoh) balls in acetone for 15 h to ensure a proper particle size distribution. Milled powders were processed in screen-printable inks by using a terpineol and ethyl-cellulose mixture and refined in a three roller mill (Exakt). The anodes were deposited on both sides of 200 μm-thick 8YSZ electrolytes (Kerafol) with 15.5 mm in diameter and sintered at 1050 ºC in air. Symmetrical cells were tested by electrochemical impedance spectroscopy using a 0 V DC – 5.0 mV AC signal in the frequency range 0.1 – 10^6 Hz. The inductive tail originated from the experimental set-up prevented the analysis at frequencies higher than 50 kHz. The measurements were carried out under different reducing atmospheres, i.e, moist hydrogen or methane (10% in Ar), and in the temperature range 650-900 ºC. Electrochemical redox cycling study entailed the treatment at 700 ºC under alternate H_2 (100%) / air (5%) atmospheres while impedance spectroscopy analysis was simultaneously carried out.

A Micromeritics system was used to carry out temperature-programmed reduction (TPR). 100 mg of sample was degassed under Ar flow for 1 h and then was subjected to reduction under H_2/Ar (1/9) flow, and heating rate of 10 K/min till 1273 K. The H_2 consumption was measured by a TCD. The reported results are normalized by the sample weight and the consumption vales are comparable among samples.

Redox cycling was monitored by means of XRD and transmission electron microscopy (TEM) in a Philips CM10 microscope. Powder reduction was carried out under continuous dry H_2 gas flow at temperatures ranging 800-900 ºC whilst re-oxidation was done under air flow at 900 ºC. Redox cycling was performed in a quartz tubular reactor. In order to identify the crystalline phase(s) of the samples, the powders were characterized by X-ray diffraction (XRD). The measurements were carried out by a PANalytical X'Pert PRO diffractometer, using CuK$\alpha_{1,2}$ radiation and an X'Celerator detector in Bragg-Brentano geometry.

Evolution of several cations on the catalyst surface has been evaluated by X-ray Photoelectron Spectroscopy (XPS) in an Specs equipment. Powdered compositions were placed on the heating chamber of the XPS and treated at 900 ºC under air, then moved to the analysis chamber and measured at room temperature. Procedure was repeated using hydrogen for reducing and air for re-oxidizing the sample, again at 900ºC in both cases.

Complementary catalytic tests were done using a fixed bed reactor for the methane steam reforming reaction under different steam to methane ratios. Activity tests were performed using 1 g of catalyst (0.25–0.42 mm particle size) diluted with SiC (0.42–0.60 mm particle size) in a volume ratio of 1:10 to avoid adverse thermal effects. The operation conditions used were: P = 1 atm, T = 600 – 900 ^oC, S/C = 1–2 H_2O mol/at. g C, W/F = 3–6 (g $_{cat}$.h/mol CH_4, $G_{total}HSV$ = 132000 h^{-1}). Prior to reaction, the catalyst was reduced in situ with 20 vol% H_2/N_2 mixture at the temperature of 900 ^oC. The reaction products were analyzed on line by gas chromatography. The gas chromatograph is constituted by two independent channels, equipped each one of them with a thermal conductivity detector. First channel allows to separate CH_4, CO, CO_2 and N_2, and the second one allows separating H_2 from the rest of constituents. Additional details concerning the testing procedure are reported elsewhere [20]. A blank experiment was performed in preliminary studies and the activity of the reactor tube (SS 310L) was negligible with respect to the activity exhibited by the present samples.

3. RESULTS AND DISCUSSION

3.1. Structural Characterization

Table 1 shows the nominal composition of the different strontium and nickel substituted lanthanum chromites synthesized by the Pechini method in this work. The optimized calcination procedure enabled the synthesis of almost single-phased materials. However, minor amounts of secondary phases are formed inevitably in the chromite synthesis [21, 22] and they can be sintering aids [23, 13], like $SrCrO_4$. These phases are present in the as-sintered materials as minor impurities, as observed in XRD patterns. Nevertheless, the main crystallographic phase of the materials is the perovskite with orthorhombic symmetry [21]. In Figure 1 and 2 these recorded patterns are shown for the synthesized materials (bottom patterns). Impurities are marked within the graph and contain mainly the aforementioned $SrCrO_4$ spinel phase, marked as *. The relative intensity of the $SrCrO_4$ peaks (e.g. the 26 and 27.5 ^{o}) decreases as nickel content increases.

The main orthorhombic perovskite is maintained even after treatment under pure dry hydrogen at 900 ºC. $SrCrO_4$ impurity diffraction peaks disappear upon reduction for all synthesized compositions (Figure 1, middle patterns). For the nickel-strontium containing perovskites (Figures 1b-1d, middle) in reduced state, peaks corresponding to metallic nickel are observed (see filled squared points in Figure 1). The relative intensity of these peaks increases as the amount of nickel in the perovskite lattice increases. Nevertheless, these metallic nickel peaks are related to the relative increase in intensity of the NiO diffraction peaks (marked as + in Figure 1) for the oxidized perovskites. Indeed, the solubility limit [15] of nickel into the perovskite lattice has been reported to be lower than 20% mol in B-site and the excess may be in the form of NiO. On the other hand, the perovskite based on the strontium-free $LaCr_{0.9}Ni_{0.1}O_{3-\delta}$ formula shows La_2O_3 diffraction peaks (Hexagonal P-3m1, ref. 00-040-1281 [24]) in the reduced status (Figure 1e middle) which is maintained after re-oxidation (Figure 1e top) but with a different crystallographic structure (Hexagonal P-3m1, ref. 00-005-0602). This indicates a lack of redox stability of this Sr-free perovskite, as previously reported for strontium-free $LaNiO_3$ perovskites [25].

The previous results by XRD, also supported by the next TPR results, allow concluding that residual impurities of the perovskites are first reduced and some of the nickel in the perovskite lattice is reduced as metallic nickel. Reduction of $SrCrO_4$ phase can follow a mechanism described elsewhere [26] into a probably amorphous phase since it disappears from the XRD signal. However, a further re-oxidation step makes this phase to appear again. A similar behavior is observed for the non-solved NiO, which reduces to metallic crystalline nickel and re-oxidizes to XRD-detectable NiO. The case of strontium-free sample is more dramatic since reducibility of lattice nickel is much higher and the reduction step leads to the destruction of the perovskite structure and La_2O_3 phase appears and it is maintained after re-oxidation. The egressed metallic nickel is not reincorporated and probably recombines as small NiO particles detected by XRD.

3.2. Temperature programmed reduction analysis

The reducibility of this series of chromites has been studied by TPR. The presence of strontium in the $LaCrO_3$ structure enables the material reduction, as can be inferred from the comparison of TPR analysis of the reference $LaCrO_3$ with the $La_{0.85}Sr_{0.15}CrO_{3-\delta}$ samples shown in Figure 3. The $LaCrO_3$ material seems not to be reduced up to 900 ºC whilst the strontium-containing $La_{0.85}Sr_{0.15}CrO_3$ presents a reduction peak at ~500 ºC. This improvement of the reducibility is principally related to the increase in the Cr^{+4} concentration in the perovskite to keep charge neutrality when lanthanum is partially substituted by Sr^{+2} cations and oxygen vacancies are formed to keep the electroneutrality, as previously described for $La_{1-x}Sr_xCrO_3$ [27]. The asymmetric shape of the hydrogen consumption profile for $La_{0.85}Sr_{0.15}CrO_3$, with a broad shoulder at low temperature, suggests the contribution of the minor impurity $SrCrO_4$ (as-prepared), as extracted from the XRD analyses (Figure 2). This impurity is not detected by the XRD pattern in the reduced powder while the reduction of Cr^{+6} species should take place at low temperatures.

For the nickel-substituted $La_{0.85}Sr_{0.15}CrO_{3-\delta}$ compositions, the main reduction peak is shifted monotonically to lower temperatures with increasing nickel contents, as seen in Figure 3, which may be in mixed oxidation states II and III, being the specific Ni^{+2}/Ni^{+3} depending on Ni and Sr stoichiometry in the perovskite lattice. This fact presumably originates from the catalytic effect of metallic nickel nanoparticles. In addition, the hydrogen consumption profile of these samples is more symmetric and wider than the nickel free $La_{0.85}Sr_{0.15}CrO_{3-\delta}$ compound one. As the nickel content increases, the amount of $SrCrO_4$ impurity decreases (Figure 2) and the small TPR contribution at low temperature appear overlapped with the main reduction peaks of these nickel containing $La_{0.85}Sr_{0.15}(Cr\text{-}Ni)O_{3-\delta}$ compounds. The broad peaks suggest that the signal must be composed of several reduction peaks but highly overlapped, i.e. different nickel and chromium species are present in the sample. Indeed, apart from chromium, nickel species could be reduced to metallic nickel, as also reported for calcium-doped lanthanum nickel chromites [28] under dry methane reduction. These species may involve (ordered from high to low reducibility): NiO and $SrCrO_4$ impurities, nickel and chromium in the outer planes of the perovskite grain and nickel in the perovskite *bulk*. In fact, the TPR profile for the $La_{0.85}Sr_{0.15}Cr_{0.8}Ni_{0.2}O_{3-\delta}$ material (Figure 3) shows that this material consumes a high amount of hydrogen in separated reduction peaks. Nickel catalytic activity towards hydrogen dissociation facilitates the reduction of chromium in the perovskite (e.g. Cr^{+4} species), as reported for the ruthenium addition to $La_{1-x}Sr_xCrO_{3-\delta}$ perovskites [29]. Furthermore, the increase of the Ni^{+2} content allows increasing [16] the Cr^{+4} concentration on the B-site of the perovskite. The TPR signal for the composition with the highest nickel content ($La_{0.85}Sr_{0.15}Cr_{0.8}Ni_{0.2}O_{3-\delta}$) splits in two major differentiated peaks. The contribution of lattice chromium reduction at high temperature is combined with contribution of cationic nickel reduction. The total hydrogen consumption is not proportionally related to the nickel content but may be also influenced by the impurities and the initial chromium oxidation state. The pattern of perovskite containing the lowest nickel content (Figure 1b) presents relatively more intense peaks of the $SrCrO_4$ impurity in Figure 2, so the total Cr^{+6} available for reduction is higher and therefore the resulting hydrogen consumption is higher than expected based on the nickel content. On the other hand, the anode with the highest nickel content consumes more hydrogen than $La_{0.85}Sr_{0.15}Cr_{0.95}Ni_{0.05}O_3$ as a consequence of the higher nickel content while it presents a lower $SrCrO_4$ contribution.

The TPR signal reduction peak area of a strontium-free $LaCr_{0.9}Ni_{0.1}O_{3-\delta}$ perovskite is similar to that of $La_{0.85}Sr_{0.15}Cr_{0.9}Ni_{0.1}O_{3-\delta}$ since they have the same nickel content, but it is slightly shifted to higher temperatures. Strontium makes it possible the chromium reduction (as for $LaCrO_3$ vs $La_{0.85}Sr_{0.15}CrO_{3-\delta}$ analysis) and oxygen vacancy formation. However, the absence of strontium inhibits the $SrCrO_4$ phase formation and the total amount of chromium for reduction is lowered, i.e, only the Cr^{+4} coming from Ni^{+2} charge compensation. Nevertheless, the hydrogen consumption should be principally related to reduction of lattice nickel. Strontium also stabilizes the nickel-containing perovskite lattice under reducing atmospheres by compensating the formation of cationic vacancies with oxygen vacancies and preventing the full reduction and subsequent egression of large amounts of nickel atoms. Nevertheless, the presence of cationic defects may have implications in the electronic and ionic conductivity as well as in the surface chemistry and catalysis of the reduced perovskite materials. On the other hand, for the strontium-free perovskite in reduced state, some La_2O_3 is formed (see Figure 1e). Similar La_2O_3 formation has been detected for strontium-free perovskites with high nickel content [25].

Reduction of $SrCrO_4$ in TPR signal is inferred from the absence of the corresponding diffraction peaks in the reduced form (Figures 1a-d). Nevertheless, metallic nickel patterns are observed in the nickel-strontium lanthanum chromites. In the reduced form, no other phases different from the orthorhombic perovskite and metallic nickel is detected. For the strontium-free composition the high reducibility of lattice nickel promotes the formation of La_2O_3, since the corresponding diffraction peaks appear after reduction. Re-oxidation of the reduced samples produces again the same diffraction pattern, i.e. $SrCrO_4$ and NiO impurities appear again. However, for the $LaCr_{0.9}NiO_{3-\delta}$ sample, the formed La_2O_3 phase upon reduction is maintained after re-oxidation.

3.3. TEM analysis

The previous observation concerning the materials evolution through redox cycling can be confirmed by TEM analysis performed on samples in initial (oxidized), reduced and re-oxidized state. The TEM images (Figure 4a-b) show the powder grains in as-sintered and re-oxidized states. A smooth and continuous grain contour is detected and it is observed for all analyzed samples. Moreover, when the Ni-containing samples are exposed to reducing atmospheres the surface is altered while no changes are detected for the $La_{0.85}Sr_{0.15}CrO_{3-\delta}$ composition as observed in Figure 4c. Nickel containing chromites in reduced state show dispersed nanosized particles on the grain surface (Figure 4d-f). Table 2 summarizes the particle size distribution. Similar results were reported for the well characterized $La_{0.85}Ca_{0.15}Cr_{0.9}Ni_{0.1}O_{3-\delta}$ perovskites for methane oxidation [30] and also in $La_{0.85}Sr_{0.15}Cr_{1-y}Ni_{y}O_{3-\delta}$ compositions for SOFC anode operation [15]. As the nickel content increases, the nickel particles become larger for the strontium containing perovskites (Figure 4d-e). Strontium allows the phase stabilization of Ni-containing lanthanum chromite under reducing atmospheres, as previously inferred from XRD analysis. Namely, the same nickel content in the perovskite but without strontium leads to the formation of a larger number of nickel nanoparticles with higher size (around 60 nm), as seen in Figure 4f, despite the fact that TPR profile (Figure 3) shows a lower reduction signal. Therefore, the lack of strontium facilitates both the nickel reduction and formation of lanthanum oxide, as previously reported for $LaNiO_{3-\delta}$ perovskites [25] and the $LaCr_{1-x}Ni_{x}O_{3}$ system [31]. A large amount of nickel from the lattice egresses as metallic nickel nanoparticles for the strontium-free reduced materials. The excess/non-compensated A-site lanthanum must be reordered as oxide in the cooling down process under hydrogen. When a re-oxidation step is carried out, some of the nickel nanoparticles are re-oxidized into NiO particles (Figure 1 top patterns). The egression of lattice nickel as metallic nanoparticles in the strontium-free chromites generates a large concentration of cationic defects, which destabilizes the structure, and leads to the formation of the La_2O_3 from the excess of lanthanum. For the strontium containing perovskites, the addition of the divalent cation generates oxygen vacancies which stabilize the rest of the lattice elements in reducing conditions, i.e. prevents the excessive nickel reduction to metallic particles and the structure destabilization. Interestingly, when these nickel-containing materials are re-oxidized no particles are observed on the surface (Figure 4b).

3.4. XPS analysis

X-ray Photoelectron Spectroscopy (XPS) measurements were carried out on as-sintered powders and in-situ reduced and re-oxidized materials. The comparison of $La_{0.85}Sr_{0.15}CrO_{3-\delta}$ and $La_{0.85}Sr_{0.15}Cr_{0.9}Ni_{0.1}O_{3-\delta}$ XPS spectra is plotted in Figure 5. The low nickel content in the $La_{0.85}Sr_{0.15}Cr_{0.9}Ni_{0.1}O_{3-\delta}$ perovskite combined with the overlapping XPS signals [32] of La3d and Ni2p prevented the study of the nickel evolution. Indeed, La3d/Ni2p spectra recorded (not shown) for both samples in oxidized, reduced and re-oxidized state remained unchanged. This fact enabled the binding energy (BE) correction for the rest of the XPS spectra. Despite the chemical difference between the two samples studied by XPS (nickel content is 10% in Cr site for the $La_{0.85}Sr_{0.15}Cr_{0.9}Ni_{0.1}O_{3-\delta}$ composition), XPS signals for Cr2p, Sr3d and O1s in oxidized and reduced states are very similar for both compositions as depicted in Figure 5.

Chromium analysis. Regarding the Cr2p XPS spectra, Cr^{+3}/Cr^{+4} contributions are difficult to distinguished due to their close binding energy values [33]. Moreover, the two observed double peaks in Figure 5a,d for the initial and re-oxidized samples suggest the presence of the Cr^{+6} and $Cr^{+3}(Cr^{+4})$ species [34]. The latter chromium species are initially present in the perovskite depending on the concentration of oxygen vacancies or on the redox state of the different cations in the perovskite lattice. The presence of Cr^{+6} species is principally ascribed to $SrCrO_4$ impurities detected by XRD. When both samples are in-situ reduced, the Cr^{+6} peak (c.a. 580 eV) disappears. This fact is in agreement with the previously observation by XRD, i.e. $SrCrO_4$ impurity under reducing atmospheres decomposes into several chromates and strontium oxides [26]. As aforementioned, the strontium presence on the lanthanum-chromite lattice stabilizes the structure under reducing atmospheres. Crystal structure is still kept under reduced state, and the charge compensation involves the formation of oxygen vacancies. In the vicinity of the chromium-oxygen vacancy, chromium cations may be polarized, as “more electronegative” species with lower effective oxidation state, such as $Cr^{+3-\delta}$ (see the 574 eV signal in the reduced spectra in Figure 5a,d assigned as $Cr^{+\delta}$ species). In the case of the nickel containing lanthanum-strontium chromite, the increase of the Cr^{+4} concentration combined with the reduction of the lattice nickel enables the $Cr^{+\delta}$ surroundings increase, as extracted from the relative peak intensity $Cr^{+3/+4}/Cr^{+\delta}$ in Figure 5a, 5d middle spectra.

Strontium analysis. The XPS spectra for the Sr3d are shown in Figure 5b,e for the redox-cycled materials. Both initial and re-oxidized samples present the same XPS spectra in where Sr oxidic [34] environment in $SrCrO_4$ and $(La\text{-}Sr)(Cr\text{-}Ni)O_{3-\delta}$ co-exists. The wider peak could be attributed to overlapped doublet [35] for $Sr3d_{5/2}$ and $Sr3d_{3/2}$, as described for LSM. The reduction of the sample impurity to other chromium and strontium [34] oxidic environments is the responsible for the different intensity in XPS Sr3d spectra, whilst the main peak is maintained (c.a. 134 eV).

Oxygen analysis. O1s XPS spectra for the redox cycled compositions are depicted in Figure 5c,f. Oxidized samples spectra show a wide peak close to 529 eV and this is related to the lattice oxygen of this kind of materials [36] coupled with some oxygen in peroxo type state [37], known also as “active oxygen” [38]. The presence of carbonates is ruled out since samples were *in situ* heated up to 900 ºC prior to XPS measurements in ultra-high vacuum. The difference arose from the XPS O1s spectra of the reduced sample. An extra peak at ca. 527 eV appears (and disappears upon re-oxidation). Relative intensity of the peaks is correlated with the relative intensity of the $Cr^{+\delta}$ and Cr^{+3}/Cr^{+4} contributions in the Cr2p spectra for nickel-free and nickel-containing compositions (Figure 5a,d). The occurrence of this low BE oxygen species can be ascribed to two different phenomena: (i) the reduction of the $SrCrO_4$ impurity may probably result in the segregation of amorphous SrO. The O1s spectra for this divalent cation oxide corresponding to the lattice oxygen can appear at lower BE values as reported for Ba-based perovskites [39]; and (ii) the reduction involves the increase in the oxygen vacancy and/or $Cr^{+\delta}$ species concentration in this multimetallic perovskite and then some oxygen can be stabilized as electropositive species in this defective oxide, yielding the 527 eV signal [40]. The spectrum for the reduced nickel-containing sample shows a higher proportion of low BE oxygen, which may be related to the higher concentration of oxygen vacancies but also cationic defects due to the formation of surface metallic nickel clusters.

3.5. Electrochemical study of electrodes in H_2 and CH_4.

Electrochemical testing has been performed on symmetrical cells by impedance spectroscopy. DC conductivity study in reducing atmospheres (moist 5% vol. H_2) revealed a total conductivity exceeding 5 S/cm at 800ºC, which is mostly related to n-type electronic transport. This level of electronic conductivity is sufficient for operation as SOFC electrode although a good current collector is required to minimize ohmic losses. The cross-section of a cell consisting of 8YSZ electrolyte, perovskite electrode and a top gold printed mesh as current collector is depicted on the SEM picture in Figure 6. The electrode polarization resistance has been determined for the different anode materials operating under hydrogen or methane. Three different moist (3% vol.) atmospheres were tested: (i) pure hydrogen, (ii) 10% hydrogen in argon and (iii) 10% methane in argon. Low methane concentration was selected for avoiding cocking issues. Then the corresponding hydrogen concentration has been chosen for comparison. The polarization resistances of each anode composition are plotted in an Arrhenius arrangement in Figure 7. The standard procedure involved the *in situ* reduction of the electrode at 900 ºC for 4 h under pure moist hydrogen gas flow. In addition, the $La_{0.85}Sr_{0.15}Cr_{0.9}Ni_{0.1}O_{3-\delta}$ anode composition was also tested after initial reduction at 800 ºC instead of 900 ºC. The absolute resistance values obtained here are significantly higher than those reported for standard Ni/YSZ anodes tested as symmetrical cells consisting of YSZ electrolytes [41, 42, 43] and further optimization of the manufacture process and electrode microstructure is required to achieve competitive electrode polarization resistances.

Base $La_{0.85}Sr_{0.15}CrO_{3-\delta}$ anode composition shows the highest polarization resistance values irrespective of the fuel atmosphere and concentration. Partial substitution of chromium by nickel yields compositions with lower polarization resistances, especially at the lowest tested temperatures. Nevertheless, the highest nickel containing anode ($La_{0.85}Sr_{0.15}Cr_{0.8}Ni_{0.2}O_{3-\delta}$)

performs similar to the nickel free electrode. The high material reducibility and the consequent high concentration of nickel nanoparticles formed on the surface [27] may result in a high density of defects in the perovskites and a reduction of the oxygen-ion conductivity. Therefore, it seems that there exists a nickel content, which minimizes the electrode polarization resistance, related to the aforementioned [15] solubility limit of nickel. On the other hand, the strontium-free $LaCr_{0.9}Ni_{0.1}O_{3-\delta}$ electrode performs worse than all the strontium-containing perovskites, irrespective of the nickel content and the fuel (Figure 7), as expected [44] from the lower ionic conductivity and low stability upon reduction, whilst TEM analysis (Figure 4e) shows well distributed nickel particles larger than 50 nm.

The limitations in the electrochemical methane activation become patent from the increase in both (1) the polarization resistance values (Figure 7) and (2) the associated activation energy, as inferred from the values obtained in 10% hydrogen and 10% methane (Figure 8). However, the relative values are maintained among the different anode compositions and the lowest values are obtained for $La_{0.85}Sr_{0.15}Cr_{0.95}Ni_{0.05}O_{3-\delta}$ and $La_{0.85}Sr_{0.15}Cr_{0.9}Ni_{0.1}O_{3-\delta}$ electrodes reduced at 900 ºC. Finally, the $La_{0.85}Sr_{0.15}Cr_{0.9}Ni_{0.1}O_{3-\delta}$ anode reduced at 800 ºC exhibits the lowest polarization resistance and activation energy values irrespective of the fuel type (Figure 7 and Figure 8).

Differences on polarization resistance values among the different compositions may stem from the distinct nature of processes limiting the performance of each anode. Figure 9 presents impedance spectra for four different anode compositions at 750 ºC under pure moist hydrogen, when initially reduced at 900 ºC. The variation of the relaxation frequencies of each process as a function of the electrode composition allows understanding[1] the changes of the different contributions to the total polarization resistance. The comparatively most

---

[1] The overlapping between several processes , the complexity of the different alternative equivalent circuits and the sensitivity to the different operating variables and electrode compositions prevented the equivalent circuit fitting.

performing electrode $La_{0.85}Sr_{0.15}Cr_{0.9}Ni_{0.1}O_{3-\delta}$ is mostly controlled by low frequencies (LF) processes, presumably ascribed to surface processes [45,46,47]. The worst electrode $LaCr_{0.9}Ni_{0.1}O_{3-\delta}$ shows (Figure 9) a much less important contribution of LF processes and is principally limited by medium frequencies (MF) processes, which might be related to coupled ion transport thorough the electrode bulk and reaction processes [48, 49, 50, 51], as expected from the limited ionic conductivity of this compound. The other two electrodes show an intermediate behavior with balanced contributions of LF and MF processes.

The activity towards fuel conversion is strongly influence by strontium and nickel content, i.e. (1) the absence of strontium limits the reduction of chromium and facilitates the metallic nickel formation while (2) excess of nickel on the perovskite lattice induces a higher chromium and nickel reduction, despite the fact that perovskite structure is stabilized with the presence of strontium. Anodes having the lowest polarization resistance values are those with relatively low nickel content, i.e., $La_{0.85}Sr_{0.15}Cr_{0.95}Ni_{0.05}O_{3-\delta}$ and $La_{0.85}Sr_{0.15}Cr_{0.9}Ni_{0.1}O_{3-\delta}$. These anodes combine sufficient ionic conductivity, proper reducibility and adequate dispersion of nickel nanoparticles on the electrode surface.

The influence of the nickel nanoparticle formation has been also studied for the $La_{0.85}Sr_{0.15}Cr_{0.9}Ni_{0.1}O_{3-\delta}$ composition by carrying out the reduction step at 800 ºC. This process led to the formation of nickel nanoparticles with lower size and higher dispersion (Figure 10 and table 2) than the same anode but reduced at higher temperature, i.e. 900 ºC. The increase of number and dispersion of nickel metallic nanoparticles achieved by avoiding the fast particle coarsening, allowed the polarization resistance to be significantly reduced under hydrogen and in a lower extent under methane (Figure 7). In this case, it can be assumed that for both electrodes the microstructure and the ionic conductivity is practically identical and, therefore, the higher dispersion and lower particle size should allow improving surface processes and not affect the other transport processes. This aspect is confirmed by Figure 11, which shows the Nyquist plots for these two anodes recorded at 750ºC in wet hydrogen. Firstly, it is observed the substantial reduction of the polarization resistance, also shown in the Arrhenius plot of Figure 7. Concerning the different contributions, the better nickel dispersion allows decreasing significantly the resistance associated to LF processes (mostly surface catalysis) and the most important contribution is shifted to MF processes.

Decreasing the hydrogen concentration from 100% to 10% involves an increase in the polarization resistance for all the compositions (compare Figure 7a-b) that becomes more important with increasing temperatures, i.e. the activation energy under 10 % H_2 is slightly lower (See Figure 8). This decrease in the activation energy values may be linked to a change in the rate limiting steps, presumably the contribution of resistive process ascribed to surface reaction should be higher under diluted hydrogen. This aspect is confirmed by the later detailed analysis of the impedance spectra in Figure 12. On the other hand, methane activation is more difficult [44] and, consequently, both the polarization resistance (Figure 7c) and the corresponding activation energies (Figure 8) increased considerably with respect to the operation under 10% H_2, as described before. The difficulty of methane activation by these anode materials is also affected by the carbon formation due to the presence of nickel [30]. Nevertheless a great advantage of these perovskite-based anodes is the possibility of regenerate the samples by a proper oxidizing gas shift, as previously suggested by XRD, TEM and XPS analyses.

Finally, the effect of the redox cycling on the electrochemical performance of $La_{0.85}Sr_{0.15}Cr_{0.9}Ni_{0.1}O_{3-\delta}$ (reduced at 800ºC) was studied. Figure 13a presents the electrode polarization resistance evolution with time at 700ºC, i.e. subjected to the in-situ cycling from reducing to oxidizing conditions. The performance deterioration is evident after the treatment in air, reaching resistance values more than one order of magnitude higher when shifting from wet hydrogen to air. However, the original performance is recovered upon switching back to wet hydrogen and even the resistance slightly decreases after the last cycles. This behavior confirms that the cycling/regeneration of the $La_{0.85}Sr_{0.15}Cr_{0.9}Ni_{0.1}O_{3-\delta}$ electrode is possible while short-term mechanical issues were ruled out, since the electrode integrity was maintained after cycling and cooling down. Representative Nyquist spectra corresponding to both oxidized and reduced state are also presented in Figure 13 (b and c). Electrode operation in oxidizing conditions is mainly limited by LF-MF processes, which might be related to electrode surface changes upon re-oxidation.

3.6. Catalytic study of CH_4 steam reforming in a fixed bed reactor.

In order to test the suitability of these anode materials for methane activation catalytic experiments for methane reforming were carried out in a fixed bed reactor. Similar experiments were performed for strontium-containing lanthanum chromites with low nickel content [52]. For the $La_{0.85}Sr_{0.15}Cr_{0.9}Ni_{0.1}O_{3-\delta}$ material the methane conversion at different temperatures and operating conditions is shown in Figure 14. The maximum methane conversion of this catalyst for the methane steam reforming was around 30% at 900 ^{o}C and for the lowest steam to methane tested ratio (S/C = 1.0). However, at low temperatures, the reforming activity increases with increasing steam to methane ratios, as can be expected but this behavior changes when the reaction temperature is higher than 800ºC. A possible explanation of these results could be found in the stability of the reduced state of nickel. The catalyst reduced at 900 ^{o}C has a higher activity than the same catalyst reduced at lower temperatures indicating a strong interaction between nickel and the support and then nickel is hard to reduce under these relatively high steam concentrations. It can be expected that reduced nickel can be oxidized easily, especially if it is in the form of highly dispersed nanoparticles, as for the sample reduced at 800 ºC (Figure 10). As a result, high steam concentrations can lead to nickel nanoparticle oxidation, lowering the surface concentration of active sites available for steam reforming reaction. The stoichiometric ratio for methane steam reforming reaction is 1:1, then an excess of water is an effective oxidant agent of nickel metal at high temperature. The reaction was stable after 600 minutes of reaction irrespective of the steam to methane ratio at 900 ºC.

4. CONCLUSIONS

Different anodes based on the $La_{1-x}Sr_xCr_{1-y}Ni_yO_{3-\delta}$ perovskitic materials have been tested on symmetrical cells under hydrogen and methane atmospheres. Redox stability of these materials has been checked by XRD, TEM and XPS and, finally, unambiguously proved by electrochemical redox cycling using symmetrical cells supported on YSZ electrolyte. Perovskite crystallographic structure is maintained upon reduction and re-oxidation. Strontium-free composition suffers from structure degradation. TEM images confirm that all nickel-containing materials present metallic nickel nanoparticles on the surface of the perovskite grains after reduction. Material re-oxidation permits these Ni nanoparticles being incorporated again into the perovskite grains and the resulting grain surface is smooth as the corresponding to the initial oxidized materials. XPS spectra for initial and re-oxidized materials coincide, as observed for the two analyzed samples $La_{0.85}Sr_{0.15}CrO_{3-\delta}$ and $La_{0.85}Sr_{0.15}Cr_{0.9}Ni_{0.1}O_{3-\delta}$. The XPS spectra of the reduced samples show differences ascribed to chromium (Cr^{+6}, Cr^{+4}/Cr^{+3}) and the consequent formation of defects in the perovskite structure. Nickel reduction to metallic nanoparticles could not be followed by XPS. Reducibility of these chromites has been tested by TPR experiments. Increase of nickel content decreases the reduction temperature whilst strontium in the lattice facilitates the whole material reduction. Methane activation is possible with these anodes materials as concluded by the calculated polarization resistance on symmetrical cells. Electrochemical impedance spectroscopy measurements allow finding that nickel content in the $La_{0.85}Sr_{0.15}Cr_{1-x}Ni_xO_{3-\delta}$ structure has an optimum value that reduces the polarization resistance. Low nickel contents are enough for increase the performance of these regenerable anodes at low temperatures. Decreasing the reduction temperature benefits the electrochemical activation of hydrogen and methane. Methane catalytic conversion for the most promising

$La_{0.85}Sr_{0.15}Cr_{0.9}Ni_{0.1}O_{3-\delta}$ material has been tested for the methane steam reforming reaction. Values of 30% of methane conversion have been found at 900 ºC and they were kept after 600 min on reaction stream. Steam concentration control is identified as a key issue for the nickel reducibility and the associated (electro-)catalytic activity for fuel conversion. The electrochemical study of cells subjected to three consecutive redox cycles demonstrated the performance recovery upon regeneration.

Acknowledgements

Authors thank funding by the Universidad Politécnica de Valencia (Grant FPI-UPV-2007-06), the Spanish Ministry for Science and Innovation (Project ENE2008-06302) and Generalitat Valenciana (Grant ACOMP2010/223). P. Concepción has contributed to this work with the XPS measurements. N. Morlanés, S. Climent and M. Algarra are kindly acknowledged for the catalytic experiments.

References

[1] http://www.hexis.com/index_e.htm; http://www.bloomenergy.com/

[2] D. B. Levin, L. Pitt, M. Love, Int. J. Hydrogen Energy 29 (2004) 173

[3] J. N. Armor, App. Catal. A 176 (1999) 159

[4] M. A. Peña, J. P. Gomez, J. L. G. Fierro, App. Catal. A 144 (1996) 7

[5] J. R. Rostrup-Nielsen, Catal. Today 71 (2002) 243

[6] D. Fouquet, A.C. Müller, A. Weber, E. Ivers-Tiffé, Ionics 8 (2003) 103

[7] A. Atkinson, S. Barnett, R. J. Gorte, J. T. S. Irvine, A. J. Mcevoy, M. Mogensen, S. C. Singhal, J. Vohs, Nat. Mater. 3 (2004) 17

[8] S. P. Jiang, S. H. Chan, J. Mater. Sci. 39 (2004) 4405

[9] W. A. Meulenberg, J. M. Serra, T. Schober, Solid State Ionics 177 (2006) 2851 - 2856

[10] S. Tao, J. T. S. Irving, Nature Materials 2 (2003) 320

[11] O. A. marina, N. L. Canfield, T. W. Stevenson, Solid State Ionics 149 (2002) 21

[12] H. Yokokawa, N. Sakai, T. Kawada, M. Dokiya, Solis State Ionics 52 (1992) 43

[13] M. Mori, Y. Hiei, N. M. Sammes, Solid State Ionics 135 (2000) 743

[14] E. V. Tsipis, V. V. Kharton, J. Solid State Electrochem. 12 (2008) 1367

[15] W. Kobsiriphat, B. D. Madsen, Y. Wang, M. Slah, L. D. Marks, S. A. Barnett, J. Electrochem. Soc. 157 (2010) B279

[16] S. Tao, J. T. S. Irvine, Solid State Ionics 179 (2008) 725–731

[17] M. Pechini, U.S. Pat. 3,330,697 (1967)

[18] J. M. Serra, V. B. Vert, M. Betz, V.A.C. Haanappel, W.A. Meulenberg, F. Tietz, J. Electrochem. Soc. 155 (2008) B207

[19] J.M. Serra, S. Uhlenbruck, W. A. Meulenberg, H. P. Buchkremer, D. Stöver, Topics Catal. 40 (2006) 123

[20] F. V. Melo, N. Morlanés, Catalysis Today 133–135 (2008) 374

[21] B. I. Lee, R. K. Gupta, C. M. Whang, Mater. Res. Bull. 43 (2008) 207

[22] D. H. Peck, M. Miller, K. Hilpert, Solid State Ionics 123 (1999) 59

[23] S. Simner, J. Ardí, J. Stevenson, T. Armstrong, J. Mater. Sci. 34 (1999) 5721

[24] X'Pert HighScore Plus software v. 2.2b; PANalytical B. V., 2006, Almelo, the Netherlands

[25] R. Pereñíguez, V. M. González-DelaCruz, J. P. Holgado, A. Caballero, Appl. Catal. B-Environ. 93 (2010) 346

[26] M. Mori, T. Yamamoto, T. Ichikawa, Y. Takeda, Solid State Ionics 148 (2002) 93

[27] A. Yan, B. Liu, B. Tu, Y. Dong, M. Cheng, S. Song, P. Tsiakaras, J. Fuel Cell Sci. Tech. 4 (2007) 79

[28] R. T. Baker, I. S. Metcalfe, App. Catal. A-Gen. 126 (1995) 319

[29] A.-L. Sauvet, J. Fouletier, F. Gaillard, M. Primet, J. Catal. 209 (2002) 25

[30] J. Sfeir, P. A. Buffet, P. Möcli, N. Xanthopoulos, R. Vasquez, H. J. Mathieu, J. Van herle, K.R. Thampi, J. Catal. 202 (2001) 229

[31] M. Stojanović, R. G. Haverkamp, C. A. Mims, H. Moudallal, A. J. Jacobson, J. Catal. 165 (1997) 315

[32] R. M. García de la Cruz, H. Falcón, M. A. Peña, J. L. G. Fierro, Appl. Catal B 33 (2001) 45

[33] R. Merryfield, M. McDaniel, G. Parks, J. Catal. 77 (1982) 348

[34] K. Rida, A. Benabbas, F. Bouremmad, M. A. Peña, A. Martínez-Arias, Catal. Commun. 7 (2006) 963

[35] Q.-H. Wu, M. Liu, W. Jaegermann, Mater. Lett. 59 (2005) 1480

[36] J. L. G. Fierro, Catal. Today 8 (1990) 153

[37] A. F. Carley, M. W. Roberts, A. K. Santra, J. Phys. Chem. B 101 (1997) 9978

[38] G. Vovk, X. Chen, C. A. Mims, J. Phys. Chem. B 109 (2005) 2445

[39] J.-H. Kim, B. Tsuchiya, S. Nagata, T. Shikama, Solid State Ionics 179 (2008) 1182

[40] A. F. Carley, M. W. Roberts, A. K. Santra, J. Phys. Chem. B 101 (1997) 9978

[41] S. P. Jiang, S. H. Chan, J. Mater. Sci. 39 (2004) 4405

[42] P. Blennow, K. K. Hansen, L. R. Wallenberg, M. Mogensen, ECS Trans. 13 (26) (2008) 181

[43] S.-W. Baek, J. Bae, Int. J. Hydrogen Energy 36 (2011) 689

[44] P. Vernoux, Ionics 3 (1997) 270

[45]. M. Mogensen, and T. Lindegaard, *in Proceedings of the Third International Symposium on Solid Oxide Fuel Cells*, S.C. Singhal and H. Iwahara, Editors, PV 94-3, p. 484, The Electrochemical Society Proceedings Series (1993).

[46] J. M. Serra, V. B. Vert, J. Electrochem. Soc. 157 (10) (2010) B1349

[47] J. M. Serra, V. B. Vert, ChemSusChem 2 (2009) 957

[48] S. Primdahl, and M. Mogensen, *J*. Electrochem. Soc. 144 (1997) 3409.

[49] S. P. Jiang, and S. P. S. Badwal, Solid State Ionics 123 (1999) 209.

[50] R. Barfod, A. Hagen, S. Ramousse, P. V. Hendriksen, and M. Mogensen, Fuel Cells 2 (2006) 141.

[51] V. Sonn, A. Leonide, and E. Ivers-Tiffée, J. Electrochem. Soc. 155 (2008) B675.

[52] A. L. Sauvet, J. T. S. Irvine, Solid State Ionics 167 (2004) 1

Table 1. Stoichiometry of the synthesized anode samples used in the text and graphs

Composition
$LaCrO_{3-\delta}$
$La_{0.85}Sr_{0.15}CrO_{3-\delta}$
$La_{0.85}Sr_{0.15}Cr_{0.95}Ni_{0.05}O_{3-\delta}$
$La_{0.85}Sr_{0.15}Cr_{0.9}Ni_{0.1}O_{3-\delta}$
$La_{0.85}Sr_{0.15}Cr_{0.8}Ni_{0.2}O_{3-\delta}$
$LaCr_{0.9}Ni_{0.1}O_{3-\delta}$

Table 2: Particle size analysis of TEM images corresponding to different anode in reduced state.

Composition	$T_{Reduction}$	mean	Std. deviation
$La_{0.85}Sr_{0.15}Cr_{0.9}Ni_{0.1}O_{3-\delta}$	800 ºC	16.0	2.6
$La_{0.85}Sr_{0.15}Cr_{0.9}Ni_{0.1}O_{3-\delta}$	900 ºC	19.7	3.0
$La_{0.85}Sr_{0.15}Cr_{0.8}Ni_{0.2}O_{3-\delta}$	900 ºC	19.5	4.9
$LaCr_{0.9}Ni_{0.1}O_{3-\delta}$	900 ºC	53.8	4.8

Figure Captions

Figure 1. XRD patterns for the synthesized anode compositions recorded at room temperature. Each plot contains the patterns for the synthesized (bottom), reduced at 900 ºC (middle) and re-oxidized (top) powders: (a) $La_{0.85}Sr_{0.15}CrO_{3-\delta}$; (b) $La_{0.85}Sr_{0.15}Cr_{0.95}Ni_{0.05}O_{3-\delta}$; (c) $La_{0.85}Sr_{0.15}Cr_{0.9}Ni_{0.1}O_{3-\delta}$; (d) $La_{0.85}Sr_{0.15}Cr_{0.8}Ni_{0.2}O_{3-\delta}$; and (e) $LaCr_{0.9}Ni_{0.1}O_{3-\delta}$. Used symbols: (+) NiO; (■) metallic Ni; (*) $SrCrO_4$; (●) La_2O_3 (upon reduction); and (○) La_2O_3 (upon re-oxidation).

Figure 2. Magnification of the XRD patterns for anode compositions as prepared. (*) for $SrCrO_4$ and the rest of peaks are assigned to the perovskite structure.

Figure 3. TPR signals for the different anode compositions synthesized.

Figure 4. TEM images for the anode powders in the initial (a) and re-oxidized state (b) for different anode compositions and treatment under hydrogen at 900 ºC (c-f).

Figure 5. XPS spectra for the $La_{0.85}Sr_{0.15}CrO_{3-\delta}$ (a-c) and $La_{0.85}Sr_{0.15}Cr_{0.9}Ni_{0.1}O_{3-\delta}$ (d-f) for the Cr2p (left), Sr3d (center) and O1s (right) regions.

Figure 6. SEM images of a fractured cross-section of a symmetrical cell after testing. The dense 8YSZ electrolyte, the porous anode layer and the Au top current collecting mesh can be seen (a). The BSE detector image (b) highlights the small amount of Au particles present on the anode layer deposited upon fracture of the sample.

Figure 7. Electrode polarization resistance (Rp) values obtained for the symmetrical cells under moist 100% hydrogen (a), (b) 10% hydrogen and 10% methane (c) for the synthesized compositions.

Figure 8.Activation energy obtained for the electrode polarization resistance for each fuel and the different andoe materials: (a) $La_{0.85}Sr_{0.15}CrO_{3-\delta}$; (b) $La_{0.85}Sr_{0.15}Cr_{0.95}Ni_{0.05}O_{3-\delta}$; (c) $La_{0.85}Sr_{0.15}Cr_{0.9}Ni_{0.1}O_{3-\delta}$; (d) $La_{0.85}Sr_{0.15}Cr_{0.8}Ni_{0.2}O_{3-\delta}$; (e) $LaCr_{0.9}Ni_{0.1}O_{3-\delta}$; and (f) $La_{0.85}Sr_{0.15}Cr_{0.9}Ni_{0.1}O_{3-\delta}$ reduced at 800 ºC.

Figure 9. Impedance Nyquist spectra for several anode compositions reduced at 900 ºC and recorded at 750 ºC under moist 100% hydrogen. Marked symbols indicate the frequency decades.

Figure 10. TEM images for the same anode powder $La_{0.85}Sr_{0.15}Cr_{0.9}Ni_{0.1}O_{3-\delta}$ composition reduced at 900 ºC (a) and 800 ºC (b) under hydrogen. The average particle size is described on each picture.

Figure 11. Impedance Nyquist spectra for the same $La_{0.85}Sr_{0.15}Cr_{0.9}Ni_{0.1}O_{3-\delta}$ anode-based symmetrical cell but when reduction was carried out at 900 or 800 ºC recorded at 750 ºC under wet 100 % hydrogen. Marked symbols indicate the frequency decades

Figure 12. Impedance Nyquist spectra of the $La_{0.85}Sr_{0.15}Cr_{0.9}Ni_{0.1}O_{3-\delta}$ electrode reduced at 800 ºC measured in symmetrical cells at 800 and 700 ºC under two different hydrogen partial pressure atmospheres. Marked symbols indicate the frequency decades.

Figure 13. Electrochemical performance of $La_{0.85}Sr_{0.15}Cr_{0.9}Ni_{0.1}O_{3-\delta}$ electrode at 700ºC subjected to 3 redox cycling in alternate wet 100% H_2/air environment. (a) Polarization resistance evolution with time and redox cycle; (b) and (c) Impedance Nyquist spectra plots corresponding to reduced and oxidized regime, respectively.

Figure 14. Reaction temperature effect on conversion in methane steam reforming reaction. Operation conditions: P = 1 atm; T = 600–900 ^{o}C; S/C = 1–2 H_2O mol/at. g C; molar ratio $CH_2/H_2O/H_2/N_2$ = 10.5–21.0/21.0/1.5/56.5–67.0; W/F = 3–6 g cat.h/mol CH_4; G_{total}HSV = 132000 h^{-1}.

Figure 1

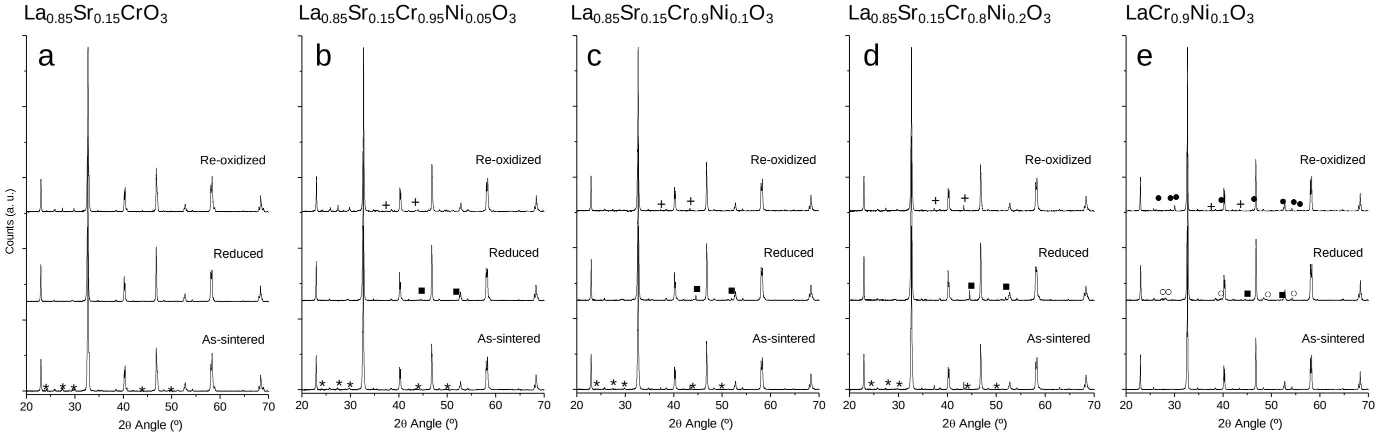
$La_{0.85}Sr_{0.15}CrO_3$
$La_{0.85}Sr_{0.15}Cr_{0.95}Ni_{0.05}O_3$
$La_{0.85}Sr_{0.15}Cr_{0.9}Ni_{0.1}O_3$
$La_{0.85}Sr_{0.15}Cr_{0.8}Ni_{0.2}O_3$
$LaCr_{0.9}Ni_{0.1}O_3$
a
b
c
d
e
Re-oxidized
Reduced
As-sintered
Counts (a. u.)
20
30
40
50
60
70
2θ Angle (º)

Figure 2

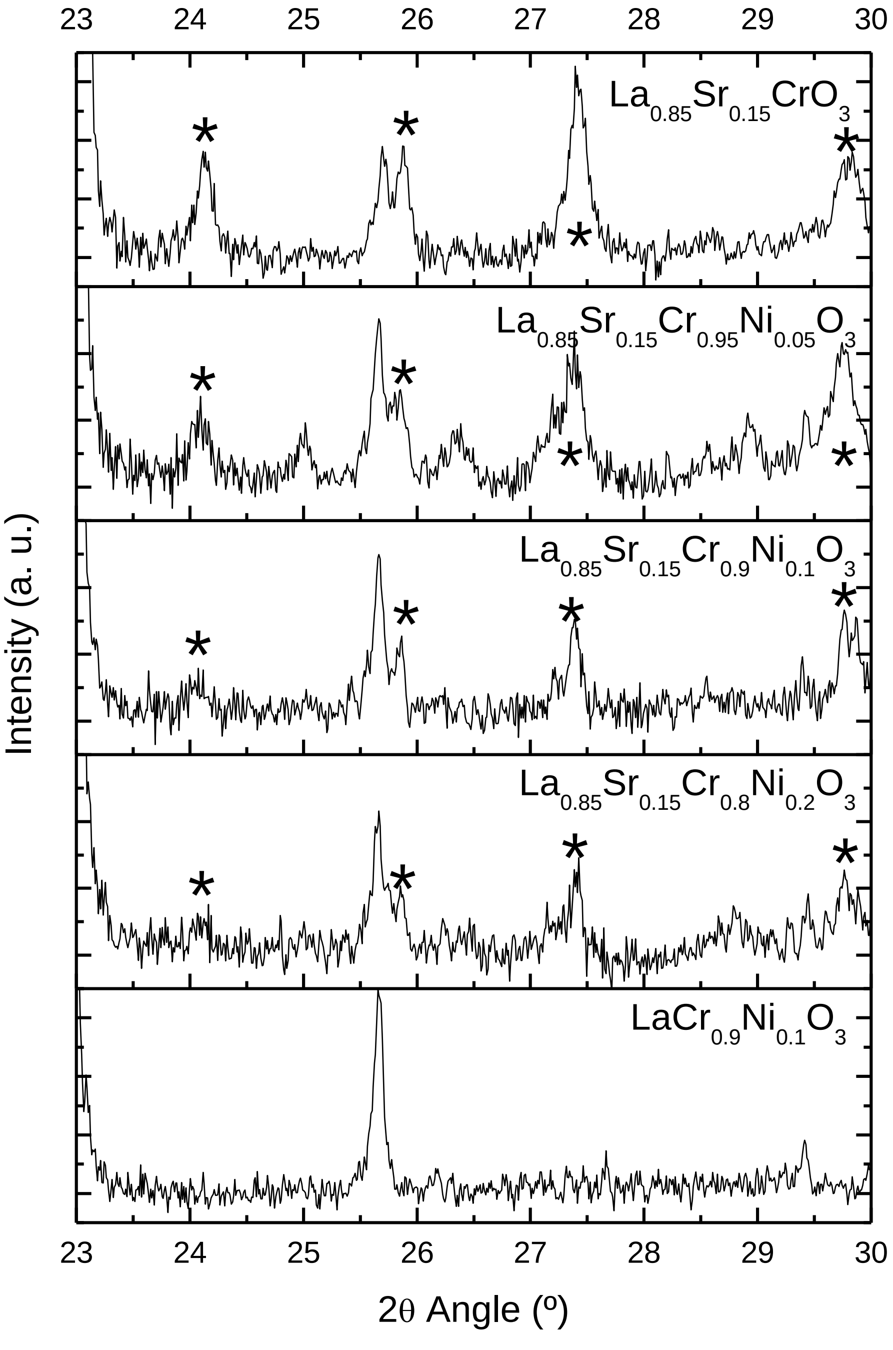
23
24
25
26
27
28
29
30
$La_{0.85}Sr_{0.15}CrO_3$
$La_{0.85}Sr_{0.15}Cr_{0.95}Ni_{0.05}O_3$
$La_{0.85}Sr_{0.15}Cr_{0.9}Ni_{0.1}O_3$
$La_{0.85}Sr_{0.15}Cr_{0.8}Ni_{0.2}O_3$
$LaCr_{0.9}Ni_{0.1}O_3$
*
Intensity (a. u.)
2θ Angle (º)

Figure 3

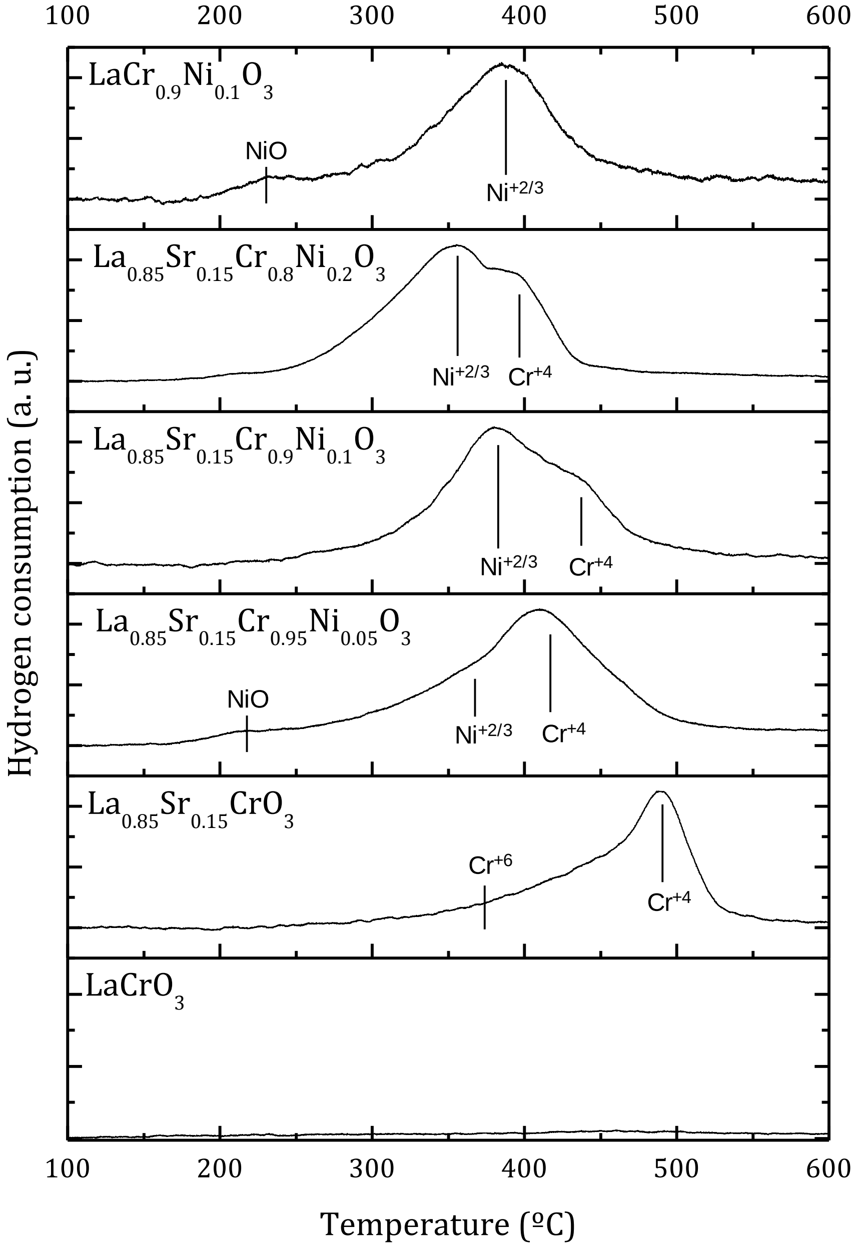
100
200
300
400
500
600
LaCr$_{0.9}$Ni$_{0.1}$O$_3$
NiO
Ni$^{+2/3}$
La$_{0.85}$Sr$_{0.15}$Cr$_{0.8}$Ni$_{0.2}$O$_3$
Ni$^{+2/3}$
Cr^{+4}
La$_{0.85}$Sr$_{0.15}$Cr$_{0.9}$Ni$_{0.1}$O$_3$
Ni$^{+2/3}$
Cr^{+4}
La$_{0.85}$Sr$_{0.15}$Cr$_{0.95}$Ni$_{0.05}$O$_3$
NiO
Ni$^{+2/3}$
Cr^{+4}
La$_{0.85}$Sr$_{0.15}$CrO$_3$
Cr^{+6}
Cr^{+4}
LaCrO$_3$
Hydrogen consumption (a. u.)
100
200
300
400
500
600
Temperature (ºC)

Figure 4

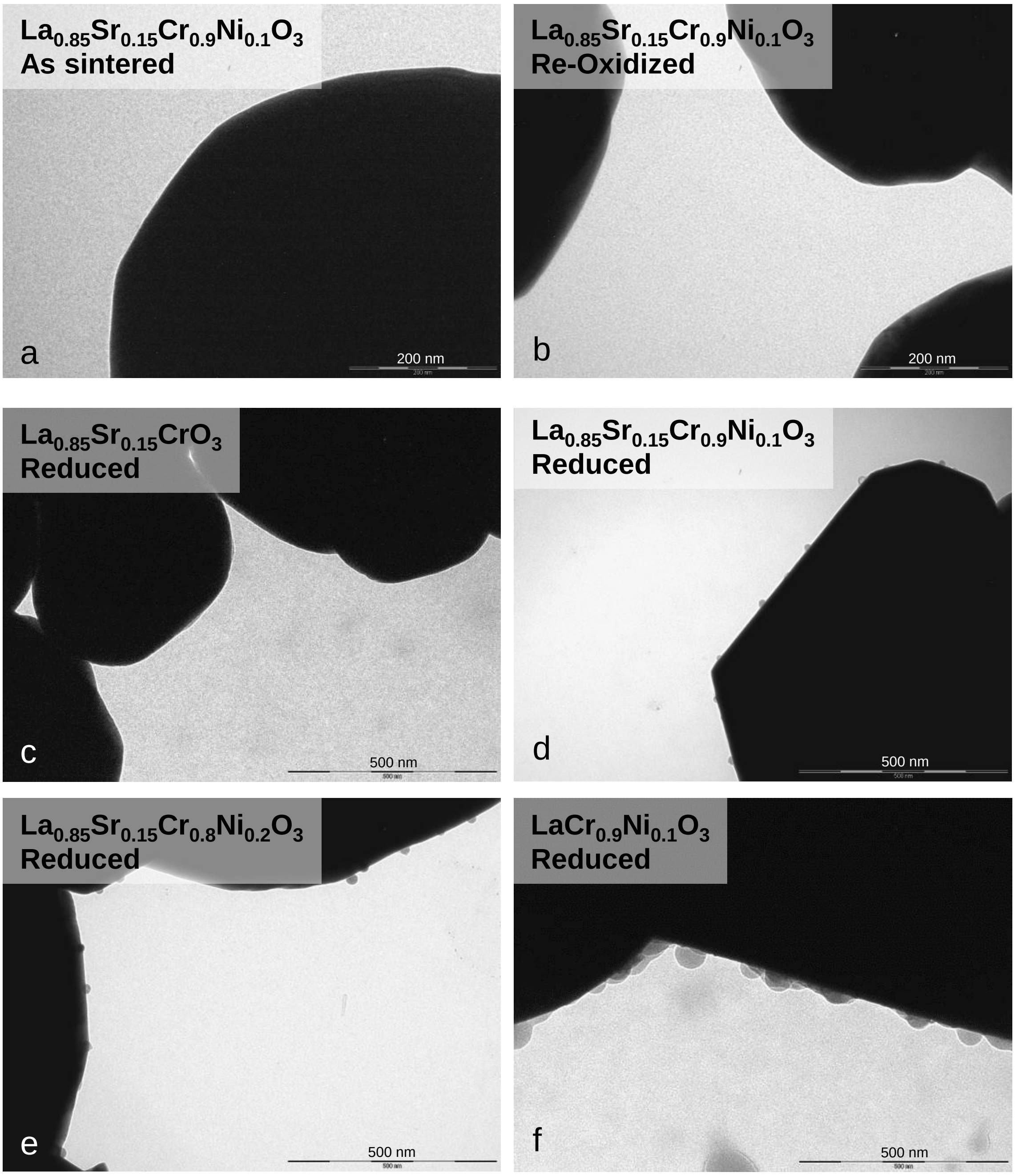
$La_{0.85}Sr_{0.15}Cr_{0.9}Ni_{0.1}O_3$
As sintered
a
200 nm
$La_{0.85}Sr_{0.15}Cr_{0.9}Ni_{0.1}O_3$
Re-Oxidized
b
200 nm
$La_{0.85}Sr_{0.15}CrO_3$
Reduced
c
500 nm
$La_{0.85}Sr_{0.15}Cr_{0.9}Ni_{0.1}O_3$
Reduced
d
500 nm
$La_{0.85}Sr_{0.15}Cr_{0.8}Ni_{0.2}O_3$
Reduced
e
500 nm
$LaCr_{0.9}Ni_{0.1}O_3$
Reduced
f
500 nm

Figure 5

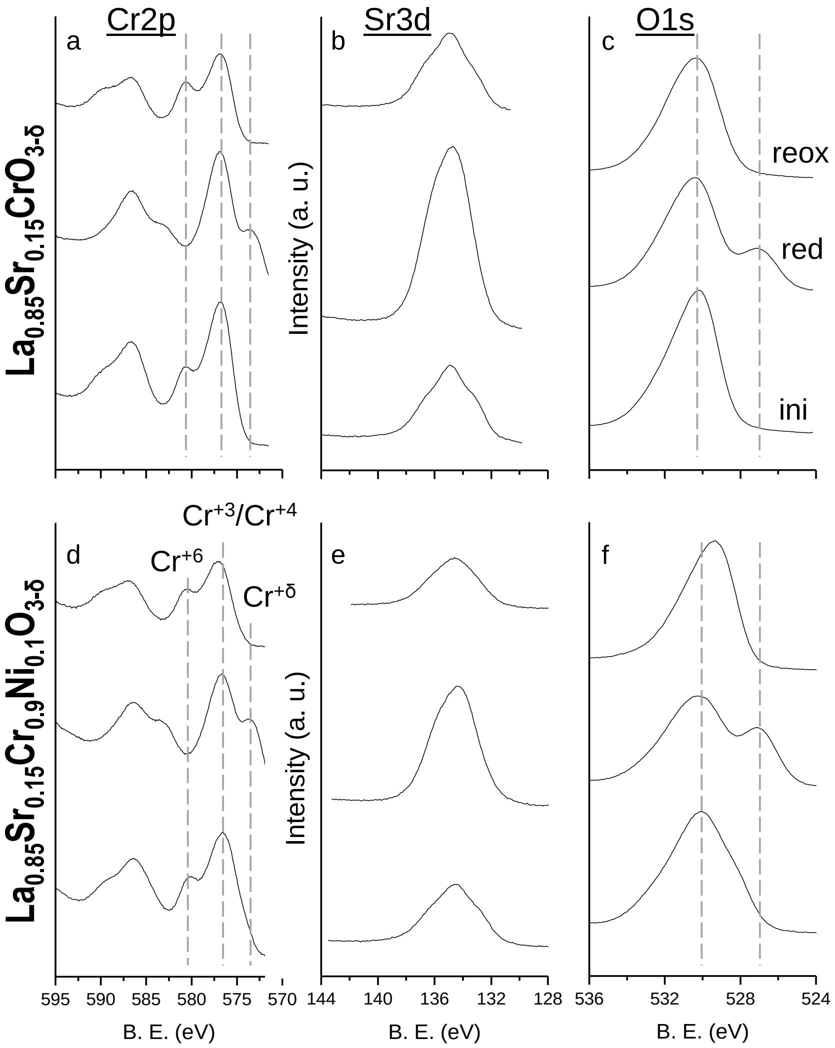
Cr2p
Sr3d
O1s
a
b
c
La0.85Sr0.15CrO3-δ
Intensity (a. u.)
reox
red
ini
Cr+3/Cr+4
d
Cr+6
Cr+δ
e
f
La0.85Sr0.15Cr0.9Ni0.1O3-δ
Intensity (a. u.)
595 590 585 580 575 570
144 140 136 132 128
536 532 528 524
B. E. (eV)
B. E. (eV)
B. E. (eV)

Figure 6

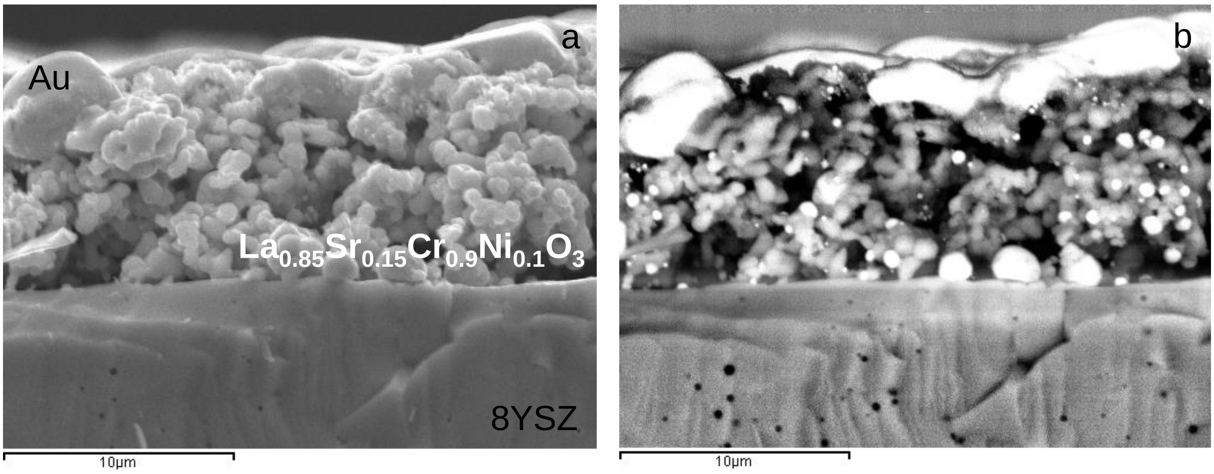

Figure 7

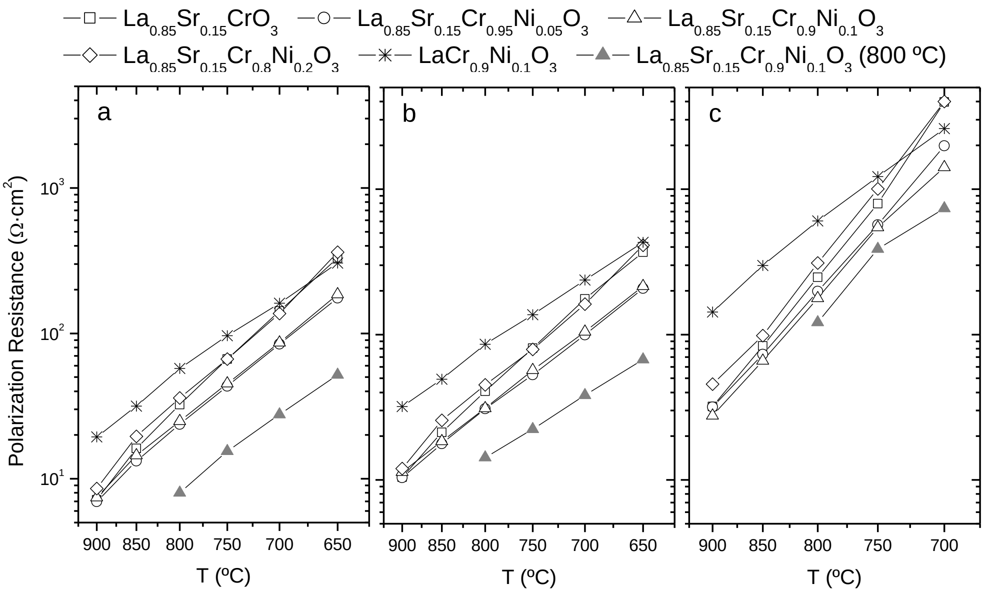

—□— $La_{0.85}Sr_{0.15}CrO_3$
—○— $La_{0.85}Sr_{0.15}Cr_{0.95}Ni_{0.05}O_3$
—△— $La_{0.85}Sr_{0.15}Cr_{0.9}Ni_{0.1}O_3$
—◇— $La_{0.85}Sr_{0.15}Cr_{0.8}Ni_{0.2}O_3$
—✳— $LaCr_{0.9}Ni_{0.1}O_3$
—▲— $La_{0.85}Sr_{0.15}Cr_{0.9}Ni_{0.1}O_3$ (800 ºC)
a
b
c
Polarization Resistance (Ω·cm^2)
10^3
10^2
10^1
900 850 800 750 700 650
900 850 800 750 700 650
900 850 800 750 700
T (ºC)
T (ºC)
T (ºC)

Figure 8

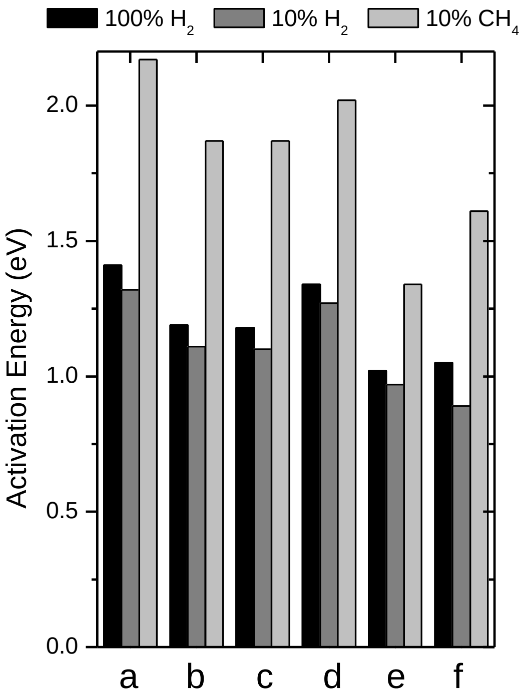

Figure 9

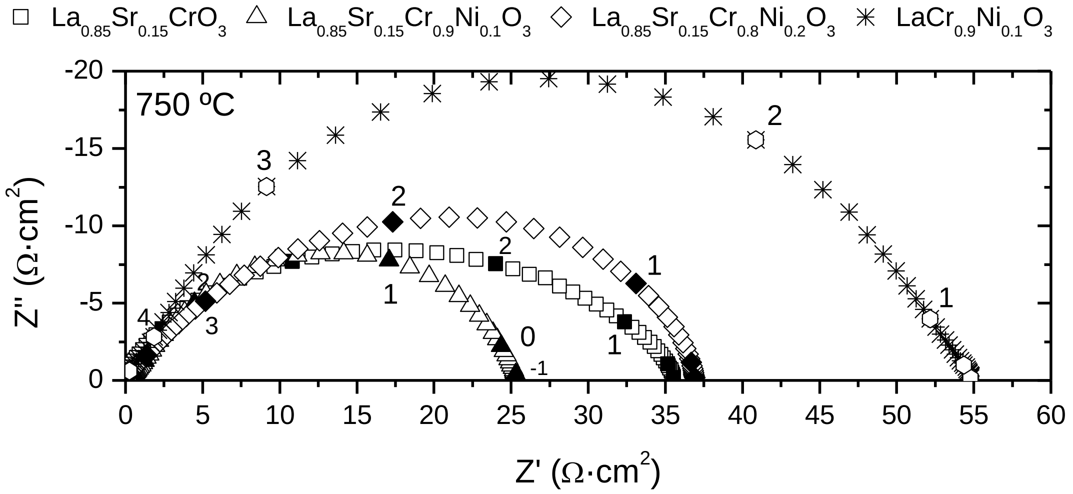
□ $La_{0.85}Sr_{0.15}CrO_3$
△ $La_{0.85}Sr_{0.15}Cr_{0.9}Ni_{0.1}O_3$
◇ $La_{0.85}Sr_{0.15}Cr_{0.8}Ni_{0.2}O_3$
✳ $LaCr_{0.9}Ni_{0.1}O_3$
750 ºC
Z'' (Ω·cm^2)
Z' (Ω·cm^2)
-20
-15
-10
-5
0
0
5
10
15
20
25
30
35
40
45
50
55
60
4
3
2
1
0
-1

Figure 10

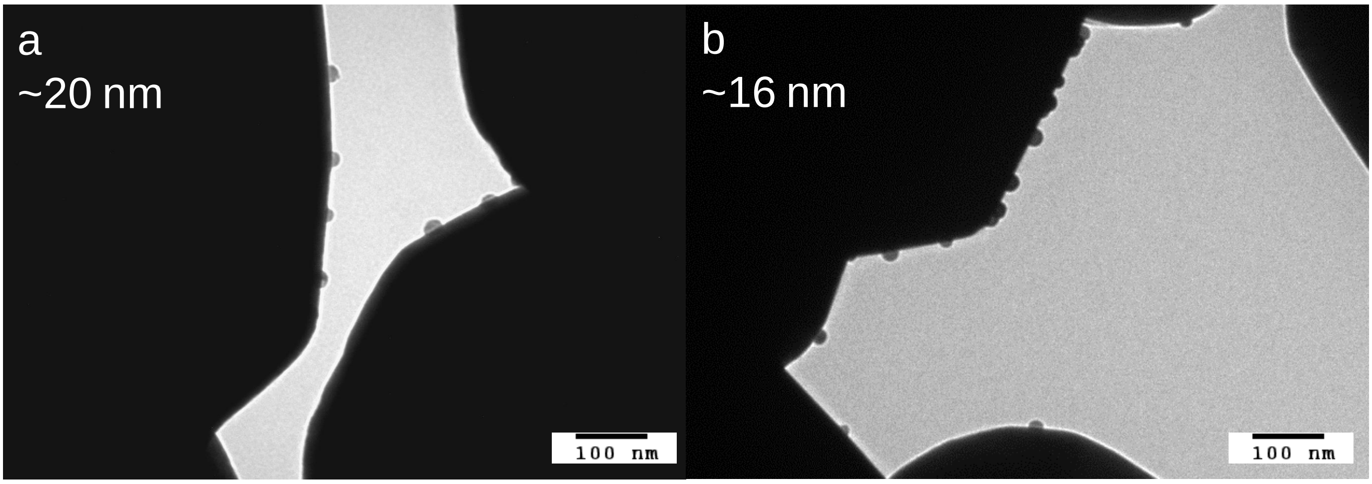

Figure 11

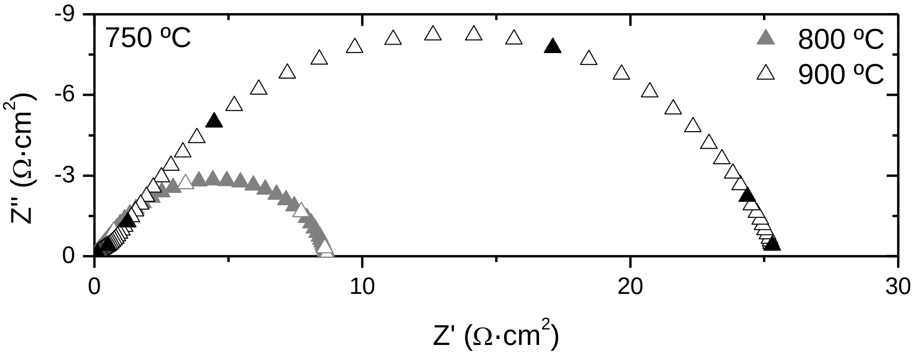

Figure 12

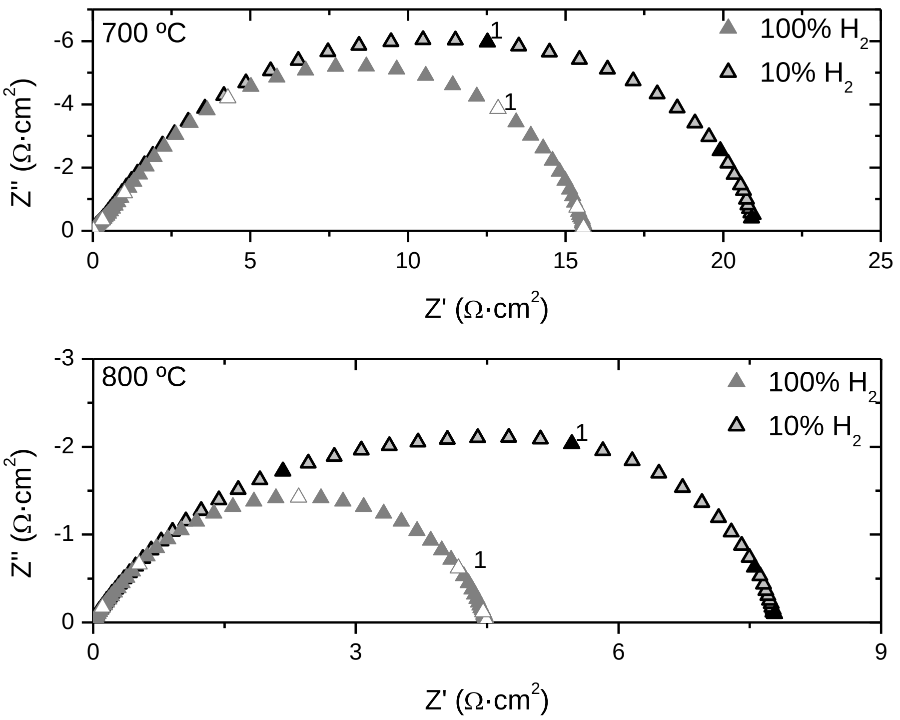
700 ºC
100% H_2
10% H_2
1
1
-6
-4
-2
0
0
5
10
15
20
25
Z'' (Ω·cm^2)
Z' (Ω·cm^2)
800 ºC
100% H_2
10% H_2
1
1
-3
-2
-1
0
0
3
6
9
Z'' (Ω·cm^2)
Z' (Ω·cm^2)

Figure 13

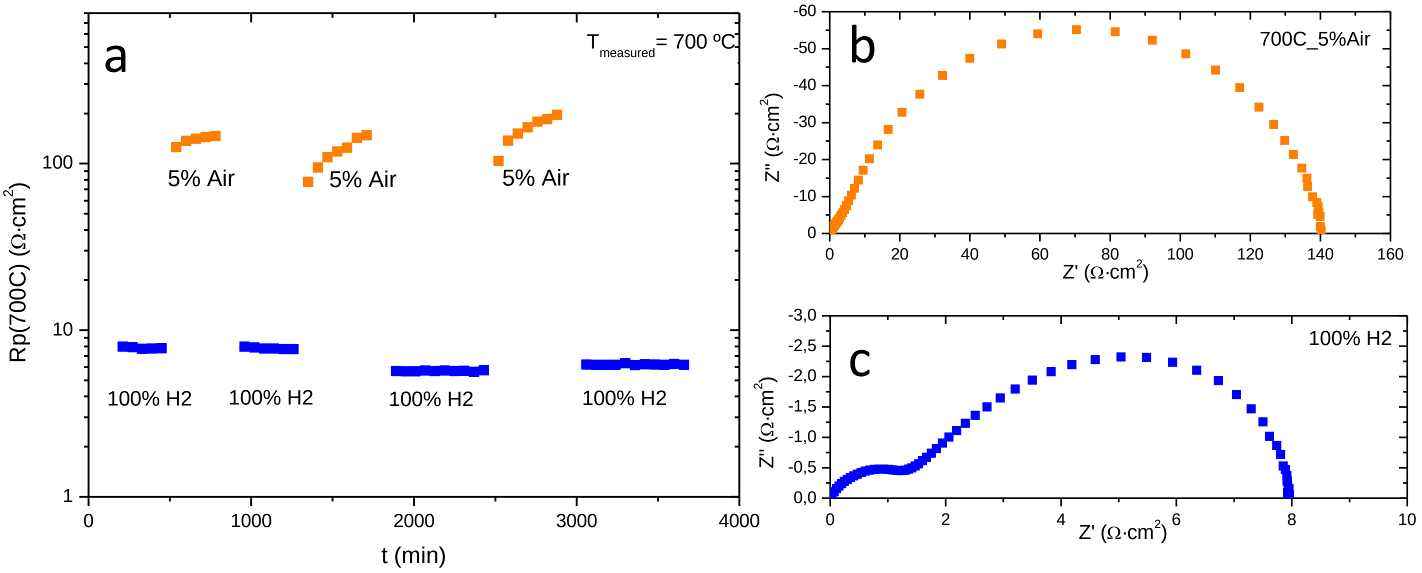
a
T measured = 700 ºC
5% Air
5% Air
5% Air
100% H2
100% H2
100% H2
100% H2
Rp(700C) (Ω·cm²)
1
10
100
0
1000
2000
3000
4000
t (min)
b
700C_5%Air
Z'' (Ω·cm²)
-60
-50
-40
-30
-20
-10
0
0
20
40
60
80
100
120
140
160
Z' (Ω·cm²)
c
100% H2
Z'' (Ω·cm²)
-3,0
-2,5
-2,0
-1,5
-1,0
-0,5
0,0
0
2
4
6
8
10
Z' (Ω·cm²)

Figure 14

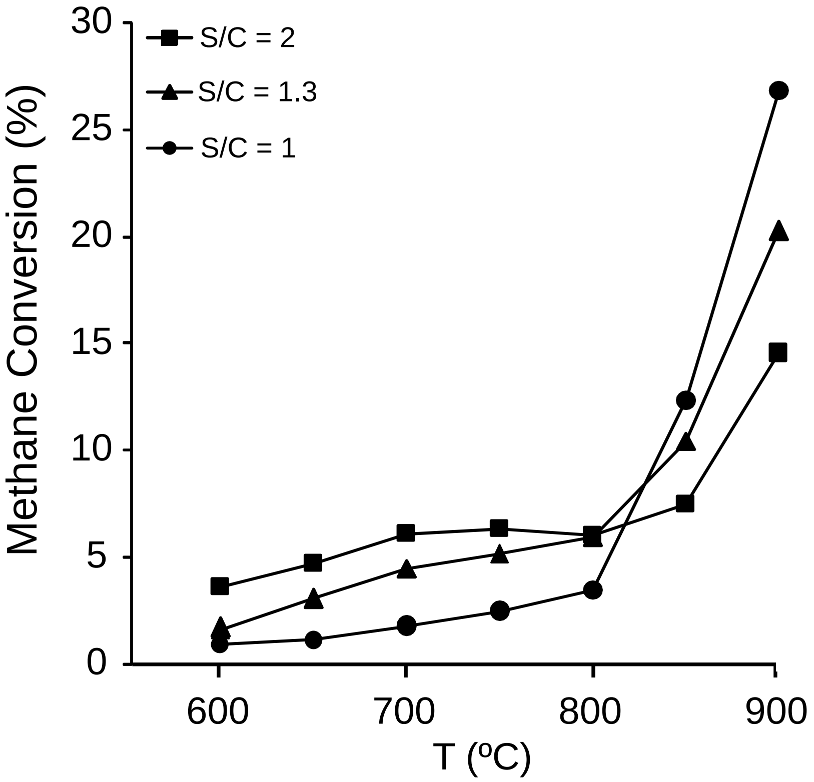

30
25
20
15
10
5
0
Methane Conversion (%)
S/C = 2
S/C = 1.3
S/C = 1
600
700
800
900
T (ºC)